The Astrophysical Journal Supplement Series, 288:7 (10pp), 2027 January https://doi.org/10.3847/1538-4365/aeb876
© 2026. The Author(s). Published by the American Astronomical Society.
OPEN ACCESS

Scale-dependent Statistics of Coherent Magnetic Structures in Early IMAP Observations

Sujan Prasad Gautam[1], Francesco Pecora[1,2], Subash Adhikari[1], Riddhi Bandyopadhyay[1], Jiaming Wang[1], Joshua Goodwill[1], William Taranto[1], Rayta Pradata[1], William H. Matthaeus[1], David J. McComas[3], Eric Christian[4], Nathan Schwadron[5], Matina Gkioulidou[6], Jamie Rankin[3], Timothy S. Horbury[7], Savvas Raptis[6], and Drew L. Turner[6]

[1] Department of Physics and Astronomy, University of Delaware, Newark, DE 19716, USA
[2] INAF-Istituto di Astrofisica e Planetologia Spaziali, Via del Fosso del Cavaliere 100, Roma, Italy
[3] Department of Astrophysical Sciences, Princeton University, Princeton, NJ 08544, USA
[4] Heliophysics Science Division, NASA Goddard Space Flight Center, Greenbelt, MD 20771, USA
[5] Los Alamos National Laboratory, PO Box 1663, Los Alamos, NM 87545, USA
[6] Johns Hopkins University Applied Physics Laboratory, Laurel, MD 20723, USA
[7] Department of Physics, Imperial College London, London, SW7 2BW, UK
Received 2026 September 21; revised 2026 October 19; accepted 2026 October 21; published 2026 November 25

Abstract

We analyze magnetic field observations from the early phase (2025 November to 2026 May) of the Interstellar Mapping and Acceleration Probe (IMAP) mission to quantify the statistical properties of helical magnetic structures and their relationship with turbulence intermittency. Structures, such as current sheets, are identified using the partial variance of increments (PVI) method, and the scale-dependent normalized magnetic helicity is computed over scales ℓ corresponding to 0.5–3 correlation lengths (λ_c). Prior studies have typically applied the PVI-helicity method to individual events; here we extend this technique to the ensemble statistics of a multimonth sample spanning many correlation times. To separate coherent helical structures from random turbulent fluctuations, significance thresholds for helicity are determined using phase-randomized surrogate realizations. We find a clear scale dependence in the occurrence, duration, and waiting time of coherent magnetic helicity, reminiscent of the scale-transfer arguments underlying inverse cascade, selective decay, and Taylor relaxation theories. Event duration and waiting-time distributions are well described by power-law and exponential models over different ranges, consistent with previous findings. In addition, PVI and magnetic helicity are anticorrelated, suggesting that high-PVI regions are preferentially associated with the boundaries of flux ropes, while their interiors tend to exhibit lower-PVI and stronger magnetic helicity.

Unified Astronomy Thesaurus concepts: Solar wind (1534); Interplanetary turbulence (830); Interplanetary magnetic fields (824); Space plasmas (1544)

1. Introduction

Coherent magnetic structures, such as magnetic discontinuities (T. S. Horbury et al. 2001; V. Zhdankin et al. 2012; A. Greco et al. 2016; S. P. Gautam et al. 2025), current sheets (S. J. Schwartz et al. 1985; G. Li 2008; O. Khabarova et al. 2015; A. Greco et al. 2018; L. Wang et al. 2025; D. L. Turner et al. 2027), and flux-tube-like structures (K.-L. Klein et al. 2008; T. V. Zaqarashvili et al. 2014; F. Pecora et al. 2019; L.-L. Zhao et al. 2019; G. P. Zank et al. 2021), are frequently observed in the turbulent solar wind over a wide range of spatial scales (A. Brandenburg et al. 2011; Q. Hu 2017; R. Chhiber et al. 2020; F. Pecora et al. 2021b). These structures are important because plasma heating (B. Somov & S. Syrovatskii 1977; R. Bowness et al. 2013; K. T. Osman et al. 2014; K. K. Reeves et al. 2019; S. P. Gautam et al. 2026), particle energization (S. L. Hess et al. 2010; O. V. Khabarova et al. 2016; H. Isliker et al. 2019; M. Nakanotani et al. 2020), and transport (R. L. Kaufmann & W. R. Paterson 2006; K.-L. Klein et al. 2008; J. Le Roux et al. 2015; H. Wu et al. 2025) can become concentrated in their vicinity and spatially organized by their presence.

A widely used diagnostic of coherent magnetic structures in spacecraft observations is the partial variance of increments (PVI; see A. Greco et al. 2008, 2012, 2018; F. Pecora et al. 2019, 2021a; R. Chhiber et al. 2020, and references therein). Previous studies (A. Greco et al. 2009; R. Chhiber et al. 2020) have shown that the temporal distribution of high-PVI structures is nonrandom, with power-law waiting times (WTs) at shorter separations and approximately exponential behavior at larger separations; their occurrence and clustering also depend on the PVI lag. Magnetic helicity provides complementary information about coherent magnetic structure by characterizing the linkage and winding of magnetic flux (H. K. Moffatt 1978; W. H. Matthaeus & M. L. Goldstein 1982). Previous studies have also shown that magnetic helicity exhibits systematic variations with spatial scale (U. Frisch et al. 1975; T. Stribling et al. 1994) and heliospheric location (J. W. Bieber et al. 1987; A. Brandenburg et al. 2011; T. Alberti et al. 2022). These studies mainly describe the broader spatial or spectral organization of helicity. To identify helical structures locally in spacecraft observations, F. Pecora et al. (2021a) developed a real-space magnetic helicity method based on the general theory provided by W. H. Matthaeus et al. (1982) and combined it with PVI. In this framework, enhanced

Original content from this work may be used under the terms of the Creative Commons Attribution 4.0 licence. Any further distribution of this work must maintain attribution to the author(s) and the title of the work, journal citation and DOI.

magnetic helicity indicates the presence of helical flux tubes, whereas strong PVI can identify sharp magnetic gradients near their internal or external boundaries.

Previous studies employing the PVI–helicity flux-tube identification method have applied it mainly to specific intervals or events (see, e.g., F. Pecora et al. 2021b). Here, we build on this work using several months of early IMAP observations from 2025 November to 2026 May. We examine structures at six different scales, from 0.5 to 3 magnetic correlation lengths, and use phase-randomized surrogate data to set a significance threshold at each scale. This allows us to study how the occurrence, duration, and WTs of helical structures change with scale, whether positive and negative helicity occur equally often, and how these structures relate to strong magnetic gradients. The statistical characterization of PVI-selected gradients and helical magnetic structures is important for understanding the local topology and dynamics of solar wind turbulence. Our contribution is therefore a statistical description of these properties across a multimonth sample, extending earlier applications of the PVI–helicity method.

2. Data and Methods

IMAP was launched in 2025 September and carries 10 instruments designed to investigate the interaction of the solar wind with the local interstellar medium and the processes responsible for particle acceleration and transport throughout the heliosphere (D. J. McComas et al. 2025). We use magnetic field and solar wind velocity measurements from early IMAP observations spanning from 2025 November 1 through 2026 May 20. Magnetic field data are obtained from the magnetometer (MAG) instrument (T. Horbury et al. 2026), while solar wind velocity measurements are obtained from the Solar Wind and Pickup Ions (SWAPI) instrument (J. Rankin et al. 2025). We use magnetic field and velocity cadences of 16 s and 60 s, respectively.

We use PVI to identify intermittent magnetic field structures. PVI measures the magnitude of the magnetic field vector increment at a given time lag τ normalized by the rms amplitude of the increments (A. Greco et al. 2018). It thus provides a pointwise measure of the strength of a magnetic field increment relative to the local level of magnetic fluctuations. For a magnetic field $\boldsymbol{B}(t)$, PVI is defined as (A. Greco et al. 2008; R. Chhiber et al. 2020),

$$\mathrm{PVI}(t,\tau)=\frac{|\Delta\boldsymbol{B}(t,\tau)|}{\sqrt{\langle|\Delta\boldsymbol{B}(t,\tau)|^2\rangle}}, \tag{1}$$

where $\Delta\boldsymbol{B}(t,\tau)=\boldsymbol{B}(t+\tau)-\boldsymbol{B}(t)$, t is the spacecraft observation time, τ is the temporal lag, and $\langle\cdots\rangle$ denotes a local average. We use an averaging window of 6 hr for our analysis. Under Taylor's hypothesis, the 6 hr averaging interval corresponds to a spatial extent along the solar wind flow of $L_{\rm avg}\simeq V_{\rm sw}\Delta t_{\rm avg}$, where $\Delta t_{\rm avg}=6$ hr. For a typical solar wind speed of 400 km s^{-1}, this gives $L_{\rm avg}\simeq 8.64\times 10^6$ km. Compared with a representative magnetic correlation length of $\lambda_c\sim 10^6$ km in our observations, the window spans about nine correlation lengths. This interval defines the local background used for PVI normalization. The PVI values are calculated at time lags of $\tau=16$, 60, and 120 s. Large PVI values (>3) correspond to fluctuations in the non-Gaussian tails of the increment distribution and are therefore associated with enhanced intermittency (W. H. Matthaeus et al. 2015; A. Greco et al. 2018; R. Chhiber et al. 2020; F. Pecora et al. 2021a).

To characterize helical magnetic structures, we estimate the local real-space magnetic helicity following the method of F. Pecora et al. (2021a, 2021b). For single-spacecraft measurements, a local estimate of the magnetic helicity at scale ℓ is obtained from the antisymmetric part of the magnetic field correlation,

$$H_m(x,\ell)=\int_0^{\ell} C(x,l)h(l)\,dl, \tag{2}$$

where

$$C(x,l)=\frac{1}{w_0}\int_{x-w_0/2}^{x+w_0/2}[b_2(\xi)b_3(\xi+l)-b_3(\xi)b_2(\xi+l)]d\xi, \tag{3}$$

and

$$h(l)=\frac{1}{2}\left[1+\cos\left(\frac{2\pi l}{w_0}\right)\right] \tag{4}$$

is a Hann window. Here, b_2 and b_3 are the magnetic field components perpendicular to the sampling direction $\hat{1}$, where $\hat{1}=\hat{2}\times\hat{3}$, and w_0 is an arbitrary interval of local integration. x denotes the position along the one-dimensional spacecraft sampling direction at which the local magnetic helicity is evaluated, and ξ is the dummy spatial coordinate used for integration over the local interval of width w_0 centered at x. We use $w_0=2\ell$. The variable l is the spatial lag entering the local correlation, whereas ℓ denotes the maximum spatial scale included in the helicity integral. We calculate H_m at six different scales, $\ell/\lambda_c=0.5$, 1.0, 1.5, 2.0, 2.5, and 3.0, where $\lambda_c=V_{\rm sw}\tau_c$ is the magnetic correlation length. The correlation time τ_c is calculated as the time at which the autocorrelation falls to a $1/e$ value (W. H. Matthaeus et al. 1998; M. E. Cuesta et al. 2022; S. P. Gautam et al. 2024).

The normalized magnetic helicity can be estimated as (F. Pecora et al. 2021b),

$$\widetilde{H}_m(x,\ell)=\frac{H_m(x,\ell)}{\langle\delta b^2\rangle\,\lambda_c}, \tag{5}$$

where $\langle\delta b^2\rangle$ is the locally averaged magnetic fluctuation energy. We estimate both $\langle\delta b^2\rangle$ and λ_c within each 6 hr analysis interval ($\Delta t_{\rm avg}=6$ hr) because this is an appropriate duration (several correlation times at 1 au, M. E. Ruiz et al. 2014; J. J. Isaacs et al. 2015; M. E. Cuesta et al. 2022) to attain statistical homogeneity. The analysis is conducted over the first 6 months of continuous coverage of the IMAP mission at Lagrange point L1.

We determine a scale-dependent threshold for estimated magnetic helicity using phase-randomized surrogate data to distinguish significant helical structures from fluctuations expected in random-phase magnetic field data, following approaches similar to those of F. Sahraoui (2008) and S. Lion et al. (2016). For each 6 hr interval, we generate 100 surrogate magnetic field time series by randomizing the Fourier phases for each component while preserving the Fourier amplitudes. This procedure preserves the power spectrum of the original

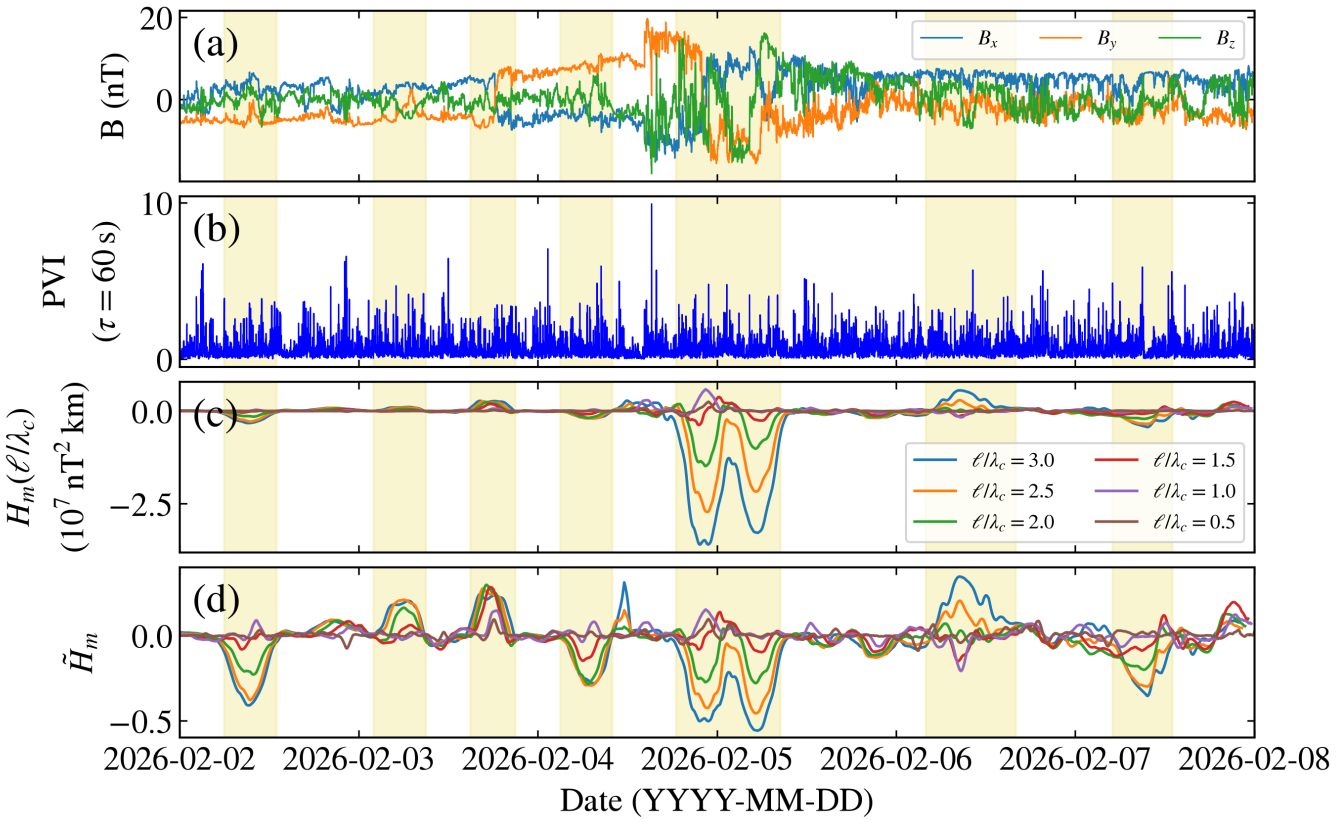


Figure 1. Example interval showing the identification of helical structures in the solar wind observed by IMAP from 2026 February 2 to 2026 February 8. From top to bottom (a)–(d), the panels show the magnetic field components, PVI at a lag of $\tau = 60$ s, scale-dependent magnetic helicity H_m, and normalized magnetic helicity $\widetilde{H}_m$ for $\ell/\lambda_c = 0.5-3.0$. The shaded regions indicate intervals containing helical structures identified against the local phase-randomized threshold.

magnetic field fluctuations while removing the phase coherence associated with coherent structures. The normalized magnetic helicity is then calculated for each surrogate. For each scale ℓ/λ_c, we construct the distribution of $|\widetilde{H}_m|$ from the phase-randomized realizations and define the threshold $H_{\rm th}$ as the 95th percentile of this distribution. Values of $|\widetilde{H}_m| > H_{\rm th}$ are therefore unlikely to arise from random-phase fluctuations and are considered as significant helical structures.

We also calculate the WT for PVI events, where consecutive samples satisfying PVI > 3 are treated as a single event. For magnetic helicity, we estimate both the WT and event duration for consecutive samples satisfying $|\widetilde{H}_m| > H_{\rm th}$. The event duration is defined as the time interval over which the event remains continuously above the corresponding threshold. The WT between two successive events is defined as $\mathrm{WT}_i = t_{\mathrm{start},i+1} - t_{\mathrm{end},i}$, where $t_{\mathrm{end},i}$ is the end of the ith event and $t_{\mathrm{start},i+1}$ is the beginning of the following event above the threshold.

3. Results

In Figure 1, we present an example interval illustrating the identification of PVI and magnetic helicity in the IMAP observations from 2026 February 2–8. Panel (a) shows the three magnetic field components, and panel (b) shows the PVI calculated at a time lag of $\tau = 60$ s. Panel (c) shows the local magnetic helicity $H_m(\ell)$ estimated at six different scales, $\ell/\lambda_c = 0.5$, 1.0, 1.5, 2.0, 2.5, and 3.0. Increasing ℓ/λ_c provides contributions from larger-scale helical structures. Panel (d) shows the corresponding normalized magnetic helicity. The real-space helicity is normalized by the local magnetic field energy. Both positive- and negative-helicity structures are evident throughout the interval, and their characteristic amplitudes and temporal extents vary with ℓ/λ_c. The shaded regions mark representative intervals identified as helical structures with normalized-helicity values larger than the local threshold. Several of these regions are also associated with enhanced-PVI activity, either at boundaries or in the interior.

Figure 2 shows the distributions of PVI calculated at different time lags of $\tau = 16$, 60, and 120 s. All three distributions are dominated by low-PVI fluctuations and are nearly identical over the low-to-moderate PVI range, but begin to separate beyond PVI ~ 3. The shortest lag shows the broadest high-PVI tail, suggesting a larger occurrence of strong intermittent fluctuations at smaller scales. Previous studies have associated PVI > 3 with non-Gaussian intermittent structures, PVI > 6 with current sheets, and PVI > 8 with possible magnetic reconnection sites (e.g., W. H. Matthaeus et al. 2015; A. Greco et al. 2018). Table 1 summarizes the occurrence of fluctuations above these thresholds. The number of events decreases gradually with increasing PVI threshold and time lag, with the strongest fluctuations occurring mostly at the shortest lag.

In Figures 3(a)–(c), we present the probability density functions (PDFs) of WT between successive PVI > 3 events for $\tau = 16$, 60, and 120 s, respectively. For all three lags, the distributions exhibit a power-law behavior at shorter WT followed by an exponential decay at longer WT. This behavior

Table 1
Occurrence of High-PVI Fluctuations at Different Time Lags

τ	PVI > 3		PVI > 6		PVI > 8	
(s)	*N*	Fraction (%)	*N*	Fraction (%)	*N*	Fraction (%)
16	17,725	1.73	1436	0.14	284	0.03
60	16,367	1.60	535	0.05	57	0.01
120	13,540	1.32	222	0.02	5	<0.001

Note. The fractions represent the percentage of the total samples at each time lag satisfying the corresponding PVI threshold.

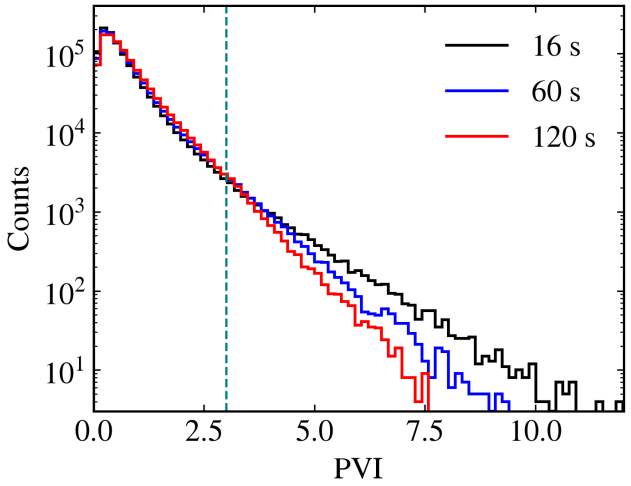


Figure 2. Distribution of PVI values calculated at time lags of $\tau = 16$, 60, and 120 s.

suggests that closely spaced intermittent structures are temporally correlated and clustered, while structures separated by longer intervals are more randomly distributed, consistent with a Poisson noise process. The mean WT, which is measured as the first moment of the distribution, increases from $\langle \mathrm{WT} \rangle = 17.5$ minutes at $\tau = 16$ s to 35.3 minutes at 60 s and 59.4 minutes at 120 s, showing that strong intermittent events become less frequent with increasing lags.

Figure 4 shows the PDFs of the absolute normalized magnetic helicity $|\widetilde{H}_m|$ for $\ell/\lambda_c = 0.5$–3.0. At the smallest scale ($\ell/\lambda_c = 0.5$), the distribution is strongly concentrated at low values of $|\widetilde{H}_m|$ and decreases rapidly toward larger helicity. As ℓ/λ_c increases, the distributions become broader and develop more extended tails toward large $|\widetilde{H}_m|$. Thus, moderate and large normalized-helicity values become gradually more common at larger scales. The vertical dashed lines indicate the scale-dependent thresholds obtained from the phase-randomized surrogate analysis. The threshold values also increase from 0.011 at $\ell/\lambda_c = 0.5$ to 0.037, 0.075, 0.123, 0.174, and 0.226 at $\ell/\lambda_c = 1$, 1.5, 2, 2.5, and 3, respectively. This increase indicates the scale dependence of the helicity fluctuations expected from the corresponding random-phase surrogate data and motivates the use of a scale-dependent threshold rather than a single fixed value.

The scale dependence evident in the PDFs is also reflected in the helicity statistics as shown in Table 2. The mean value of $|\widetilde{H}_m|$ increases from 0.016 at $\ell/\lambda_c = 0.5$ to 0.102 at $\ell/\lambda_c = 3$. The occurrence of moderately and strongly helical fluctuations also increases significantly with scale. For example, the fraction of samples with $|\widetilde{H}_m| > 0.25$ increases from 0.11% at

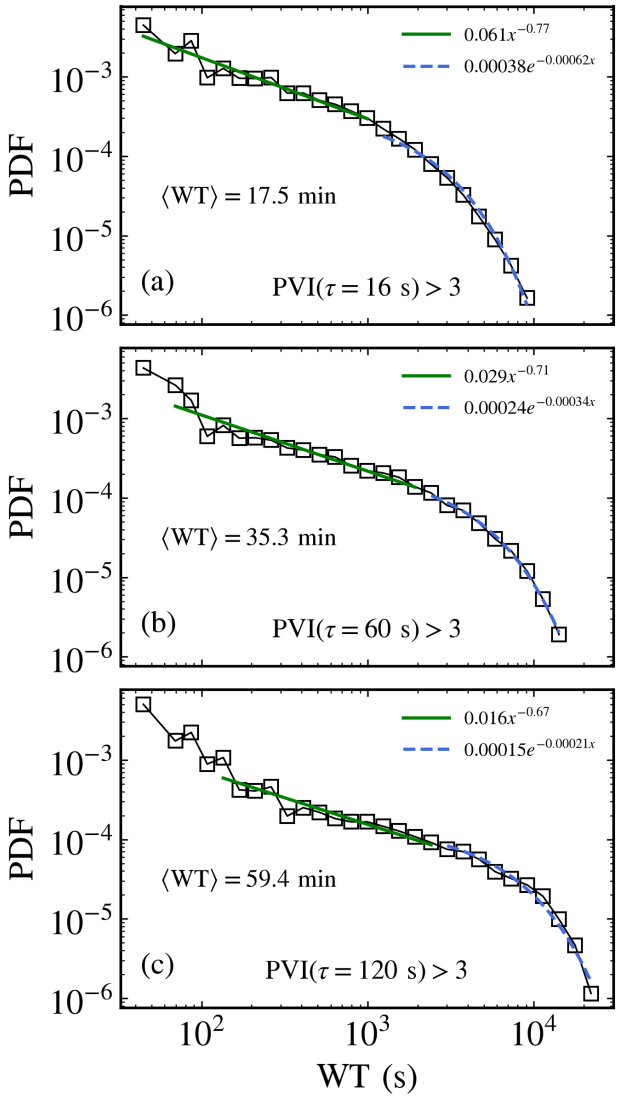


Figure 3. Probability density functions of waiting times (WTs) between successive PVI events with PVI > 3, calculated at time lags of $\tau = 16$ s (a), 60 s (b), and 120 s (c). The green solid lines show power-law fits to the shorter waiting-time (WT) regime, while the blue dashed lines show exponential fits to the longer WT tail. The corresponding mean WT $\langle \mathrm{WT} \rangle$ is shown in each panel.

$\ell/\lambda_c = 0.5$ to 9.69% at $\ell/\lambda_c = 3$, a factor of almost 90. These results demonstrate that large normalized-helicity fluctuations become gradually more common with increasing spatial scale. When the scale-dependent significance thresholds are applied, however, the fraction of samples identified as significant helical structures decreases with increasing scale. The above-threshold fraction decreases from 37.85% at $\ell/\lambda_c = 0.5$% to

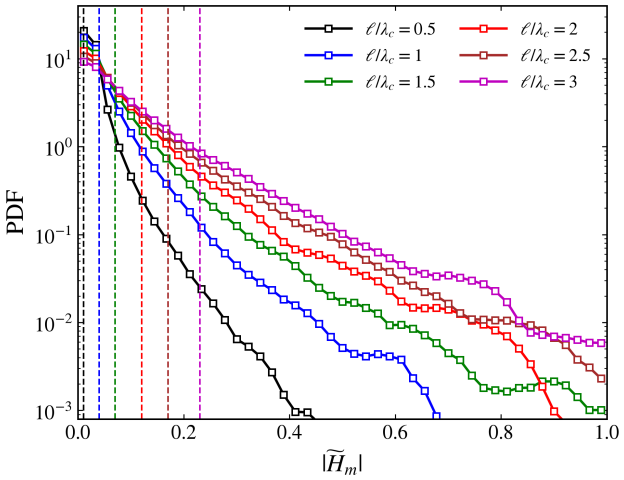


Figure 4. PDFs of the absolute normalized magnetic helicity $|\widetilde{H}_m|$ for scales $\ell/\lambda_c = 0.5$–3.0. The vertical dashed lines indicate the corresponding scale-dependent threshold values used to identify significant helical structures.

Table 2
Scale-dependent Statistics of Normalized Magnetic Helicity

ℓ/λ_c	$H_{\rm th}$	$\langle\lvert\widetilde{H}_m\rvert\rangle$	$f_{0.25}$ (%)	$f_{0.50}$ (%)	$f_{0.75}$ (%)	$\langle\lvert\widetilde{H}_m\rvert\rangle_{\rm th}$	$f_{\rm th}$ (%)
0.5	0.011	0.016	0.11	0.01	0.00	0.034	37.85
1.0	0.037	0.033	0.78	0.08	0.02	0.087	27.32
1.5	0.075	0.050	2.16	0.28	0.05	0.152	20.51
2.0	0.123	0.068	4.24	0.67	0.14	0.227	15.80
2.5	0.174	0.085	6.75	1.09	0.28	0.306	13.01
3.0	0.226	0.102	9.69	1.70	0.46	0.377	11.64

Note. $H_{\rm th}$ is the scale-dependent threshold. $\langle|\widetilde{H}_m|\rangle$ denotes the mean absolute normalized magnetic helicity calculated using all samples, whereas $\langle|\widetilde{H}_m|\rangle_{\rm th}$ denotes the mean calculated only for samples satisfying $|\widetilde{H}_m| > H_{\rm th}$. $f_{\rm th}$ is the corresponding fraction of samples above the threshold. The quantities $f_{0.25}$, $f_{0.50}$, and $f_{0.75}$ denote the percentages of samples satisfying $|\widetilde{H}_m| > 0.25$, 0.50, and 0.75, respectively.

11.64% at $\ell/\lambda_c = 3.0$, while the mean $|\widetilde{H}_m|$ of the above-threshold samples increases from 0.034 to 0.377. Thus, although large values of normalized helicity become more prevalent at larger scales, the corresponding significance criterion also becomes more restrictive because the surrogate-derived threshold increases with scale.

Figure 5 compares the statistical properties of positive- and negative-helicity structures as a function of ℓ/λ_c. Panel (a) shows the fraction of positive-helicity events, $N_+/(N_+ + N_-)$, with the horizontal dashed line marking 0.5 (equal occurrence of positive- and negative-helicity events). The fraction remains close to 0.5 across all scales, indicating no strong preference for either helicity sign, although a modest decrease in the positive-helicity fraction is observed at the largest scales. Panels (b) and (c) compare the mean event durations and WTs, respectively. The mean durations of both helicity signs increase with scale and are comparable at smaller scales, whereas negative-helicity structures tend to have slightly longer durations for $\ell/\lambda_c \gtrsim 2$. The mean WT also increases with scale, with negative-helicity structures generally showing longer WT than positive-helicity structures at the larger scales.

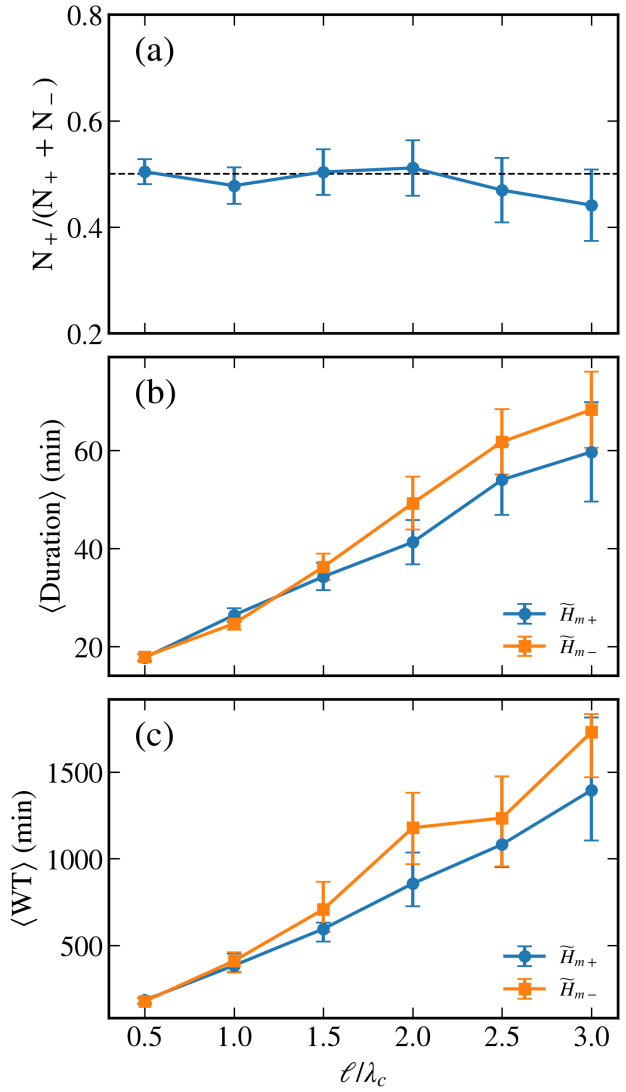


Figure 5. (a) Fraction of positive-helicity structures, $N_+/(N_+ + N_-)$, as a function of ℓ/λ_c. The dashed line is the fraction corresponding to 50%. (b) Mean duration, ⟨Duration⟩, of positive ($\widetilde{H}_{m+}$) and negative ($\widetilde{H}_{m-}$) helicity structures. (c) Mean waiting time, ⟨WT⟩, between successive positive- and negative-helicity structures. Error bars indicate the corresponding standard deviation.

Figures 6(a)–(f) show the PDFs of the durations of helical structures at different scales ($\ell/\lambda_c = 0.5$–3). At all scales, the distributions exhibit a power-law behavior at shorter durations, followed by a more rapid, approximately exponential decrease at longer durations. The fitted power-law indices show relatively little variation with scale, ranging from about −0.60 to −0.67. In contrast, the duration distributions extend progressively toward longer times as ℓ/λ_c increases. Accordingly, the mean event duration increases from $\langle T\rangle = 17.8$ minutes at $\ell/\lambda_c = 0.5$ to 64.5 minutes at $\ell/\lambda_c = 3.0$. This scale dependence indicates that helical structures identified at larger spatial scales generally persist for longer periods. In a similar format, Figure 7 shows the PDFs of the WTs between successive helical structures. The WT distributions also exhibit similar fitting trends to the event duration distributions. The short WT power-law slope becomes gradually steeper with increasing ℓ/λ_c, changing from approximately −0.22 at $\ell/\lambda_c = 0.5$ to −0.96 at

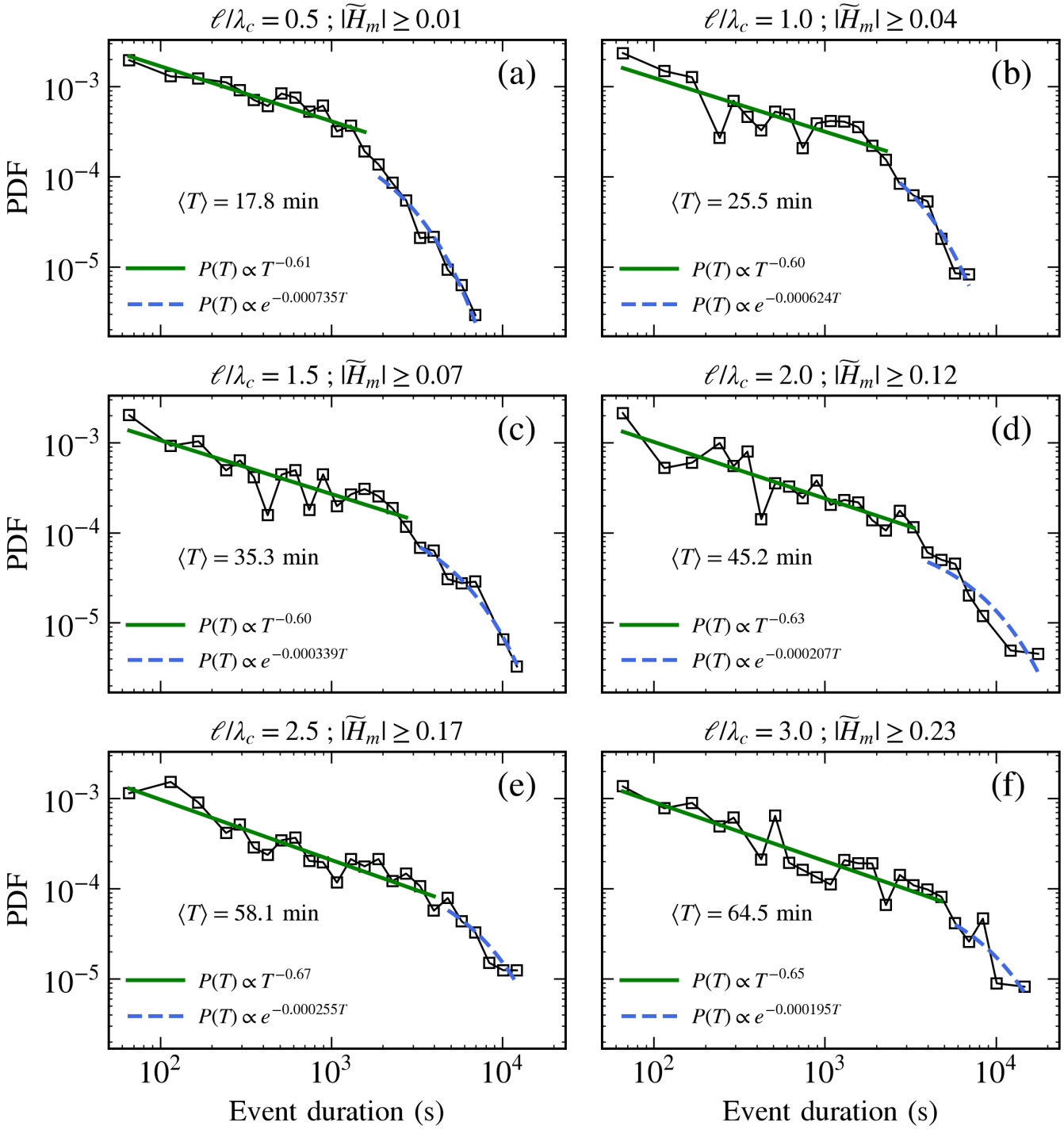


Figure 6. (a)–(f) PDFs of the durations of helical structures at scales $\ell/\lambda_c = 0.5$–3.0. The green solid lines show power-law fits to the shorter-duration regime, while the blue dashed lines show exponential fits to the longer-duration tail. The corresponding mean duration is also provided in each panel.

$\ell/\lambda_c = 3.0$. The distributions also extend toward longer WTs as the scale increases. Accordingly, the mean WT increases from $\langle \mathrm{WT} \rangle = 183.8$ minutes at $\ell/\lambda_c = 0.5$ to 1431.7 minutes at $\ell/\lambda_c = 3.0$. This increasing trend indicates that helical structures at larger scales are more widely separated in time and therefore occur less frequently. We note that although the duration and WT PDFs exhibit qualitatively similar behavior, our analysis of their joint probability distribution (not shown here) reveals no significant relationship between the duration of a helical structure and the WT between successive structures. Thus, longer-lived structures are not necessarily followed by longer or shorter WTs.

We further examine the PVI–helicity relationship. In this framework, extrema of the local magnetic helicity tend to identify the cores of helical structures, whereas enhanced PVI is preferentially associated with sharp magnetic gradients near their boundaries. Thus, large values of PVI and $|\widetilde{H}_m|$ are not necessarily expected to occur

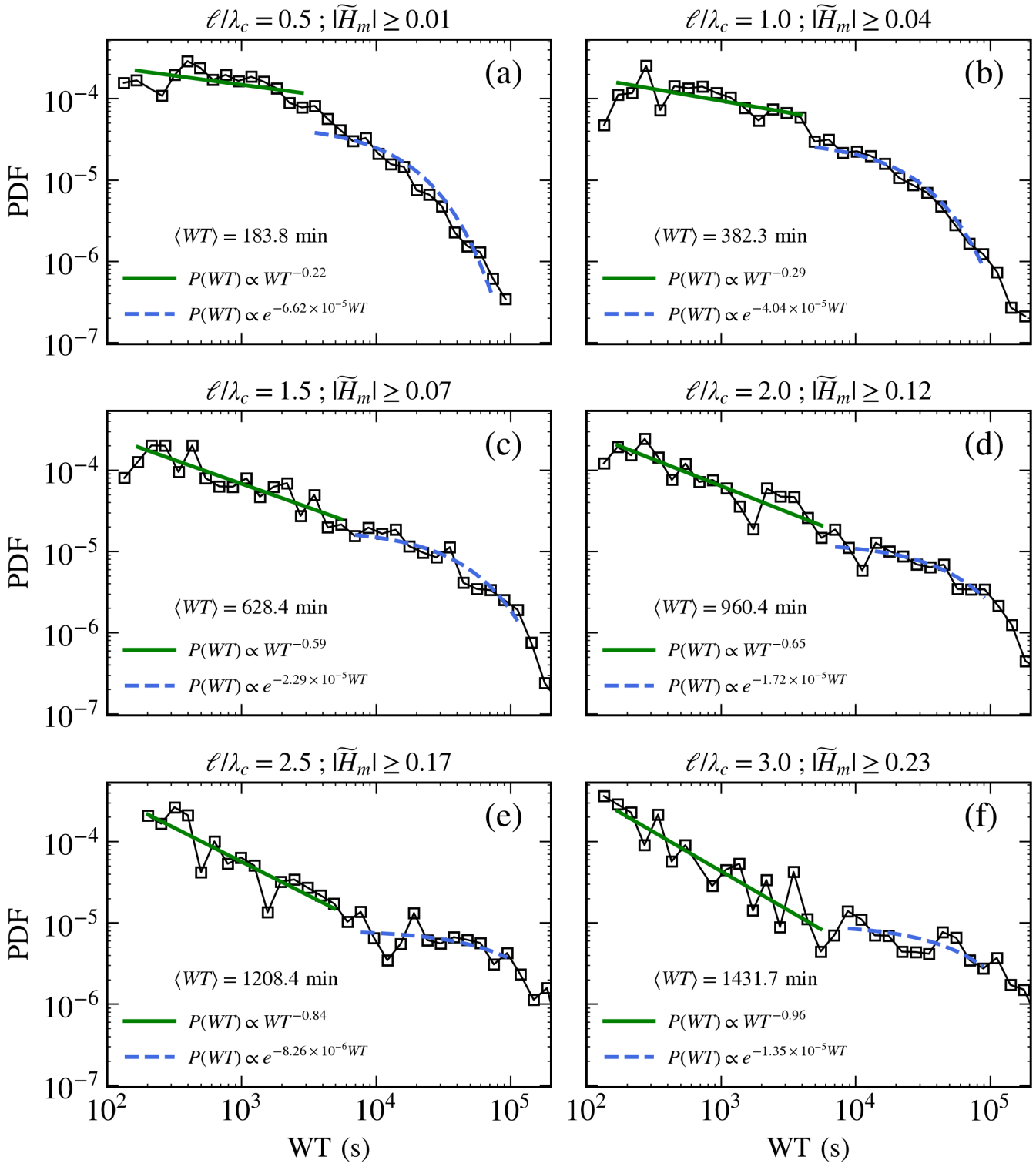


Figure 7. Same as Figure 6, but showing the PDFs of the waiting times between successive helical structures.

simultaneously, and in fact their occurrences are more likely to be anticorrelated. We consider PVI at $\tau = 60$ s and $|\widetilde{H}_m|$ at $\ell/\lambda_c = 1.5$ for this analysis. Figure 8 shows the joint probability distribution of PVI and $|\widetilde{H}_m|$. The vertical dashed line marks the helicity threshold $H_{\rm th} = 0.075$. The distribution is strongly concentrated at low PVI and low $|\widetilde{H}_m|$, while the probability decreases toward larger values of either quantity. Large PVI fluctuations occur mostly at relatively small $|\widetilde{H}_m|$, whereas samples with enhanced $|\widetilde{H}_m|$ are concentrated mainly at lower PVI. This behavior is qualitatively consistent with the picture of F. Pecora et al. (2021a), in which helicity maxima occur within relatively PVI-quiet regions and enhanced PVI marks nearby boundaries of the helical structures.

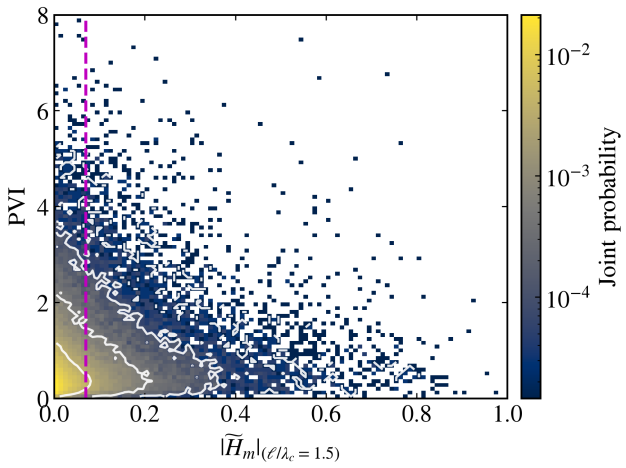


Figure 8. Joint probability distribution of PVI and $|\widetilde{H}_m|$ at $\ell/\lambda_c = 1.5$. White contours indicate levels of constant joint probability. The vertical magenta dashed line marks the helicity threshold used to identify significant helical structures at $\ell/\lambda_c = 1.5$.

4. Discussion and Conclusions

We use early IMAP observations to examine coherent magnetic structures from two complementary perspectives: (i) strong magnetic field gradients identified by PVI, and (ii) locally helical structures identified from the real-space magnetic helicity. A consistent picture emerging from the analysis is that both populations are strongly organized by scale. The high-PVI tail becomes less populated as the PVI lag increases, while the characteristic strength, duration, and separation of helical structures change systematically with ℓ/λ_c. An important aspect of the helicity analysis is that the background level itself is scale dependent. Although large values of $|\widetilde{H}_m|$ become more common toward larger scales, the surrogate-derived significance threshold also increases with scale. Consequently, a single fixed helicity threshold would not provide an equivalent significance criterion at different ℓ/λ_c (as shown in Table 2). The main results of the present analysis are summarized schematically in Figure 9. Panel (a) illustrates the physical picture in which a helical magnetic structure is bounded by sharp magnetic field gradients identified by enhanced PVI. Panel (b) summarizes the scale-dependent organization of the helical structures and the WTs between successive structures. Panel (c) shows a representative IMAP interval in which the helicity signatures at different spatial scales are viewed together with the PVI.

The observed PVI WT distributions are consistent with previous results near Earth and closer to the Sun (A. Greco et al. 2009; R. Chhiber et al. 2020), showing power-law behavior at shorter separations and an approximately exponential tail at larger separations. The estimated mean WTs are comparable to near 1 au timescales (see A. Greco et al. 2009, and references therein) and longer than those reported during Parker Solar Probe's (PSP) first perihelion (R. Chhiber et al. 2020). The shorter WTs observed by PSP may reflect the smaller turbulence correlation scales and more rapidly varying magnetic structures in the young solar wind, which evolve and become more widely separated as the solar wind expands toward 1 au.

The duration statistics of magnetic helicity provide a connection with previous flux-rope studies. Small-scale magnetic flux ropes identified at 1 au have been found to span durations from several minutes to several hours and to exhibit scale-dependent occurrence statistics (J. Zheng & Q. Hu 2018; H. Farooki et al. 2024). More recently, B. Lynch et al. (2023) applied the H_m–PVI technique to slow-to-moderate solar wind at 1 au and reported mean coherent-structure durations of approximately 1 hr. This is comparable to the mean duration found here at the largest scales, where $\langle T \rangle$ approaches 1 hr.

The present analysis further shows that the characteristic duration of helical structures at scale ℓ changes with ℓ/λ_c, while the short-duration power-law index remains relatively similar across the scales considered. This suggests that the characteristic size of the structures changes significantly with scale even though the statistical form of the short-duration population is comparatively similar. The WT statistics further show that the temporal spacing of the helicity-selected structures also depends strongly on scale. This statistical behavior is represented conceptually in Figure 9(b), where structures identified at different spatial scales occupy different temporal extents and successive helical structures are separated by finite WTs. The increasing characteristic duration and WT with ℓ/λ_c therefore indicate a systematic scale-dependent organization of the coherent magnetic structures. The power-law behavior at shorter WT followed by an exponential tail resembles the statistical organization previously reported for magnetic discontinuities (A. Greco et al. 2009; R. Chhiber et al. 2020). An additional possible interpretation of these ensemble statistics is suggested by the superposition framework of N. A. Schwadron et al. (2010). In that framework, an observed distribution may arise from the superposition of individual stochastic realizations characterized by different local parameters or occurrence rates. In particular, a superposition of Poisson-like processes having different rates can produce power-law-like WT statistics even when the individual realizations have exponential WT distributions. The solar wind intervals sampled here likely represent a range of local turbulence and coherent-structure conditions, and therefore such a superposition may contribute to the observed duration and WT distributions. Establishing a quantitative connection, however, would require characterizing the distributions of the individual realizations and relating them to the corresponding ensemble statistics, which is beyond the scope of the present study. The joint PVI–helicity statistics are also consistent with the complementary interpretation proposed by F. Pecora et al. (2021a). As summarized in Figure 9(a), enhanced helicity mainly characterizes the interior of the coherent structure, whereas large PVI values preferentially mark sharp gradients near its boundaries. The representative IMAP interval in Figure 9(c) provides an observational example of this organization, with scale-dependent helicity enhancements occurring predominantly within comparatively PVI-quiet intervals and strong PVI enhancements appearing near the boundaries of the helical structures.

We find nearly comparable occurrence rates of positive- and negative-helicity structures over the scales examined. This should not be interpreted as contradicting earlier observations of hemispheric helicity preferences (J. W. Bieber et al. 1987; A. Brandenburg et al. 2011). Those studies concern still larger-scale averaged helicity organized relative to the heliographic hemisphere, whereas the present analysis characterizes local helical structures sampled near 1 au. Interestingly, although the

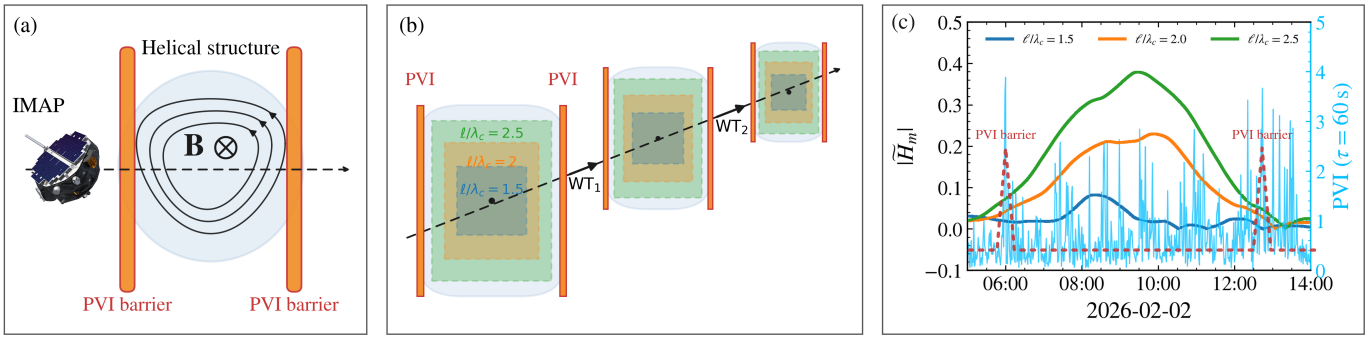


Figure 9. Summary illustration of the relationship between magnetic helicity structures and intermittent PVI events: (a) illustration of a helical magnetic structure bounded by enhanced-PVI regions, (b) schematic representation of scale-dependent helical structures and the WTs between successive structures, and (c) a representative IMAP interval of $|\widetilde{H}_m|$ at different spatial scales together with PVI calculated at a lag of 60 s.

occurrence of the two signs remains approximately balanced, differences in their durations and WTs become more evident at larger scales. Whether this asymmetry is persistent or depends on solar wind type, magnetic sector, or position relative to the heliospheric current sheet will require a larger IMAP dataset that better samples solar magnetic polarities.

By extending the PVI–helicity method to several months of early IMAP observations, we show how the statistical properties of helical structures vary with scale when identified using surrogate-based significance thresholds. As the dataset grows, the same analysis can be applied to different solar wind types, magnetic sector, heliospheric current sheet proximity, transient activity, heliocentric distance, and solar activity phase to better understand the scale-dependent properties reported here. The broader IMAP instrument suite will also permit the identified helical structures and their PVI-rich boundaries, shown schematically in Figure 9, to be related to solar wind plasma properties, energetic particle populations, and composition. Such studies are particularly relevant in view of previous evidence that helical flux tubes can act as particle-transport barriers (A. Seripienlert et al. 2010; F. Pecora et al. 2021a).

Acknowledgments

This research was partially supported by the NASA IMAP project 80GSFC19C0027 at Princeton, under a subcontract SUB0000317 at the University of Delaware and in part by the PSP/IS⊙IS project through subcontract SUB0000165 and from Princeton, as well as NSF SHINE grant AGS-2501387, and by NSF SHINE 2501387 at the University of Delaware. F.P. was partially supported by Agenzia Spaziale Italiana (ASI) in the framework of the project "Radial Evolution of large- and KInetic-scale Processes in the Expanding Solar wind (REKIPES)" C83C25000900005. J.G. was supported by the Delaware NASA Space Grant program grant number 80NSSC20M0045 at the University of Delaware. R.B. acknowledges support from NSF FDSS Award No. AGS-2347952. IMAP magnetometer operations are funded by the UK Space Agency (grant UKRI2494). T.S.H. is supported by STFC grant UKRI1202.

ORCID iDs

Sujan Prasad Gautam https://orcid.org/0000-0001-7379-4268
Francesco Pecora https://orcid.org/0000-0003-4168-590X
Subash Adhikari https://orcid.org/0000-0003-2160-7066
Riddhi Bandyopadhyay https://orcid.org/0000-0002-6962-0959
Jiaming Wang https://orcid.org/0009-0008-8723-610X
Joshua Goodwill https://orcid.org/0000-0002-5354-1164
William Taranto https://orcid.org/0009-0004-8086-3013
Rayta Pradata https://orcid.org/0009-0005-9366-6163
William H. Matthaeus https://orcid.org/0000-0001-7224-6024
David J. McComas https://orcid.org/0000-0001-6160-1158
Eric Christian https://orcid.org/0000-0003-2134-3937
Nathan Schwadron https://orcid.org/0000-0002-3737-9283
Matina Gkioulidou https://orcid.org/0000-0001-9979-2164
Jamie Rankin https://orcid.org/0000-0002-8111-1444
Timothy S. Horbury https://orcid.org/0000-0002-7572-4690
Savvas Raptis https://orcid.org/0000-0002-4381-3197
Drew L. Turner https://orcid.org/0000-0002-2425-7818

References

Alberti, T., Narita, Y., Hadid, L., et al. 2022, A&A, 664, L8
Bieber, J. W., Evenson, P., & Matthaeus, W. H. 1987, GeoRL, 14, 864
Bowness, R., Hood, A. W., & Parnell, C. E. 2013, A&A, 560, A89
Brandenburg, A., Subramanian, K., Balogh, A., & Goldstein, M. L. 2011, ApJ, 734, 9
Chhiber, R., Goldstein, M. L., Maruca, B. A., et al. 2020, ApJS, 246, 31
Cuesta, M. E., Chhiber, R., Roy, S., et al. 2022, ApJL, 932, L11
Farooki, H., Noh, S. J., Lee, J., et al. 2024, ApJS, 271, 42
Frisch, U., Pouquet, A., Léorat, J., & Mazure, A. 1975, JFM, 68, 769
Gautam, S. P., Adhikari, L., Zank, G. P., Silwal, A., & Zhao, L. 2024, ApJ, 968, 12
Gautam, S. P., Zank, G. P., Pitňa, A., & Wang, B. 2026, ApJ, 1006, 80
Gautam, S. P., Zank, G. P., Pitňa, A., et al. 2025, ApJ, 989, 82
Greco, A., Chuychai, P., Matthaeus, W. H., Servidio, S., & Dmitruk, P. 2008, GeoRL, 35, L19111
Greco, A., Matthaeus, W. H., Perri, S., et al. 2018, SSRv, 214, 1
Greco, A., Matthaeus, W. H., Servidio, S., & Dmitruk, P. 2009, PhRvE, 80, 046401
Greco, A., Perri, S., Servidio, S., Yordanova, E., & Veltri, P. 2016, ApJ, 823, L39
Greco, A., Valentini, F., Servidio, S., & Matthaeus, W. 2012, PhRvE, 86, 066405
Hess, S. L., Delamere, P., Dols, V., Bonfond, B., & Swift, D. 2010, JGRA, 115, A06205
Horbury, T., O'Brien, H., Greenaway, C., et al. 2026, SSRv, 222, 44
Horbury, T. S., Burgess, D., Fränz, M., & Owen, C. J. 2001, GeoRL, 28, 677
Hu, Q. 2017, ScChD, 60, 1466
Isaacs, J. J., Tessein, J. A., & Matthaeus, W. H. 2015, JGRA, 120, 868
Isliker, H., Archontis, V., & Vlahos, L. 2019, ApJ, 882, 57
Kaufmann, R. L., & Paterson, W. R. 2006, JGRA, 111, A10214
Khabarova, O., Zank, G., Li, G., et al. 2015, ApJ, 808, 181
Khabarova, O. V., Zank, G. P., Li, G., et al. 2016, ApJ, 827, 122
Klein, K.-L., Krucker, S., Lointier, G., & Kerdraon, A. 2008, A&A, 486, 589

Le Roux, J., Zank, G., Webb, G., & Khabarova, O. 2015, ApJ, 801, 112
Li, G. 2008, ApJL, 672, L65
Lion, S., Alexandrova, O., & Zaslavsky, A. 2016, ApJ, 824, 47
Lynch, B., Viall, N., Higginson, A., et al. 2023, ApJ, 949, 14
Matthaeus, W. H., & Goldstein, M. L. 1982, JGR, 87, 6011
Matthaeus, W. H., Goldstein, M. L., & Smith, C. 1982, PhRvL, 48, 1256
Matthaeus, W. H., Smith, C. W., & Oughton, S. 1998, JGR, 103, 6495
Matthaeus, W. H., Wan, M., Servidio, S., et al. 2015, RSPTA, 373, 20140154
McComas, D. J., Christian, E. R., Schwadron, N. A., et al. 2025, SSRv, 221, 100
Moffatt, H. K. 1978, Magnetic Field Generation in Electrically Conducting Fluids (Cambridge Univ. Press)
Nakanotani, M., Zank, G. P., & Zhao, L. 2020, JPhCS, 1620, 012014
Osman, K. T., Matthaeus, W. H., Gosling, J. T., et al. 2014, PhRvL, 112, 215002
Pecora, F., Greco, A., Hu, Q., et al. 2019, ApJL, 881, L11
Pecora, F., Servidio, S., Greco, A., & Matthaeus, W. 2021a, A&A, 650, A20
Pecora, F., Servidio, S., Greco, A., et al. 2021b, MNRAS, 508, 2114
Rankin, J., McComas, D., Alimaganbetov, M., et al. 2025, SSRv, 221, 108
Reeves, K. K., Török, T., Mikić, Z., Linker, J., & Murphy, N. A. 2019, ApJ, 887, 103
Ruiz, M. E., Dasso, S., Matthaeus, W. H., & Weygand, J. M. 2014, SoPh, 289, 3917
Sahraoui, F. 2008, PhRvE, 78, 026402
Schwadron, N. A., Dayeh, M., Desai, M., et al. 2010, ApJ, 713, 1386
Schwartz, S. J., Chaloner, C. P., Christiansen, P. J., et al. 1985, Natur, 318, 269
Seripienlert, A., Ruffolo, D., Matthaeus, W., & Chuychai, P. 2010, ApJ, 711, 980
Somov, B., & Syrovatskii, S. 1977, SoPh, 55, 393
Stribling, T., Matthaeus, W. H., & Ghosh, S. 1994, JGR, 99, 2567
Turner, D. L., Raptis, S., Horbury, T., et al. 2027, ApJS, in press
Wang, L., Wang, Y., Wei, F., et al. 2025, ApJ, 985, 113
Wu, H., Guo, Y., Keppens, R., et al. 2025, ApJ, 992, 81
Zank, G. P., Nakanotani, M., Zhao, L., et al. 2021, ApJ, 913, 127
Zaqarashvili, T. V., Vörös, Z., Narita, Y., & Bruno, R. 2014, ApJL, 783, L19
Zhao, L.-L., Zank, G., Chen, Y., et al. 2019, ApJ, 872, 4
Zhdankin, V., Boldyrev, S., Mason, J., & Perez, J. C. 2012, PhRvL, 108, 175004
Zheng, J., & Hu, Q. 2018, ApJL, 852, L23